

BrainVista: Modeling Naturalistic Brain Dynamics as Multimodal Next-Token Prediction

Xuanhua Yin¹ Runkai Zhao^{1*} Lina Yao^{2,3} Weidong Cai^{1*}

¹ The University of Sydney, Australia

² University of New South Wales, Australia

³ CSIRO's Data61

xuanhua.yin@sydney.edu.au runkai.zhao@sydney.edu.au lina.yao@unsw.edu.au
tom.cai@sydney.edu.au

Abstract

Naturalistic fMRI characterizes the brain as a dynamic predictive engine driven by continuous sensory streams. However, modeling the causal forward evolution in realistic neural simulation is impeded by the timescale mismatch between multimodal inputs and the complex topology of cortical networks. To address these challenges, we introduce BrainVista, a multimodal autoregressive framework designed to model the causal evolution of brain states. BrainVista incorporates Network-wise Tokenizers to disentangle system-specific dynamics and a Spatial Mixer Head that captures inter-network information flow without compromising functional boundaries. Furthermore, we propose a novel Stimulus-to-Brain (S2B) masking mechanism to synchronize high-frequency sensory stimuli with hemodynamically filtered signals, enabling strict, history-only causal conditioning. We validate our framework on Algonauts 2025, CineBrain, and HAD, achieving state-of-the-art fMRI encoding performance. In long-horizon rollout settings, our model yields substantial improvements over baselines, increasing pattern correlation by 36.0% and 33.3% on relative to the strongest baseline Algonauts 2025 and CineBrain, respectively.

1. Introduction

The Blood-Oxygen-Level-Dependent (BOLD) signal in functional magnetic resonance imaging (fMRI) is fundamentally a temporal process, adhering to causal dynamics where current states constrain future dynamics rather than exist-

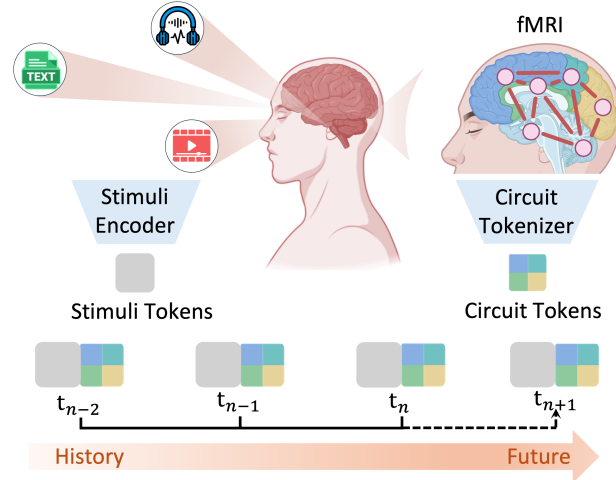


Figure 1. Naturalistic fMRI is framed as time-aligned prediction of future brain activity from recent brain history together with sensory context, modeling sequential brain activity by conditioning on past brain tokens and aligned stimuli to recursively simulate future trajectories.

ing as independent observations (Granger, 1969; Geweke, 1982). Beyond simple autocorrelation, this temporal dependency reflects the brain's operation as a predictive engine (Friston, 2005; Clark, 2013), continuously reconciling intrinsic neural dynamics with incoming sensory evidence. This coupling is particularly pronounced during dynamic stimulus processing, such as movie viewing, where neural activity emerges from the interplay of continuous sensory forcing and endogenous state propagation (Logothetis et al., 2001). Consequently, we conceptualize BOLD evolution as a non-autonomous dynamical system, where the system trajectory is conditioned on the joint history of latent brain states and temporally antecedent external stimuli.

Despite this causality, prevailing brain foundation models

*Corresponding authors.

predominantly employ masked reconstruction or bidirectional attention mechanisms (Ortega Caro et al., 2024; Dong et al., 2024; 2025). While effective for learning representations, these non-causal objectives permit information leakage from future time steps, rendering them ill-suited for modeling neural dynamics. Specifically, bidirectional conditioning creates a training-inference mismatch in autoregressive forecasting. The reliance on global context during training violates the causal constraints required for simulation, ultimately degrading the fidelity of predicted dynamics.

While autoregressive modeling with causal attention has demonstrated strong long-horizon performance in language and time-series domains (Liu et al., 2025; 2024; Wu et al., 2023; Nie et al., 2023; Brown et al., 2020), extending this paradigm to naturalistic fMRI is non-trivial. The key hurdle lies in maintaining strict causality across the mismatched timescales of high-frequency visual stimuli and slow, hemodynamically delayed BOLD signals (Lahner et al., 2024; Chang et al., 2022). Consequently, naive synchronization or feature aggregation induces look-ahead bias, inadvertently leaking future sensory content into current brain predictions. Beyond temporal fidelity, effective modeling must respect the cortex’s functional and architectural heterogeneity. The brain is organized into specialized networks that manifest conserved functional organization (Glasser et al., 2016; Finn et al., 2015; Gratton et al., 2018), while hierarchical differences in local circuit properties shape large-scale dynamics (Demirtaş et al., 2019; Wang et al., 2025a; Darvishi Bayazi et al., 2024). Generic time-sequence frameworks often fail to capture this complexity, forcing overly homogeneous representations that blur functional boundaries. This spatial smoothing obscures the directed cross-network information flow critical for decoding inter-regional connectivity.

To bridge this gap, we propose **BrainVista**, a time-aligned multimodal forecasting framework for predicting naturalistic fMRI responses from stimuli in a consistent and scalable manner, as shown in Fig. 2. To address cortical functional heterogeneity, we design **Network-wise Tokenizers** as MLP autoencoders trained to self-reconstruct fMRI signals within each functional network, producing compact token sequences that improve cross-subject transfer and long-horizon stability. To ensure strict temporal validity in multimodal conditioning, we introduce **Stimulus-to-Brain (S2B) masking**, which enforces a constraint to prevent temporal leakage and keep conditioning temporally consistent across training and inference. Accordingly, each prediction is conditioned only on the stimulus history available up to the current time step. To model directional cross-network communication without blurring functional boundaries, we further introduce a **Spatial Mixer Head**. It explicitly controls cross-network mixing, instead of relying on implicit global attention that can over-smooth cross-ROI spatial activation patterns and reduce network-specific contrast. We

evaluate BrainVista on three public naturalistic fMRI benchmarks, Algonauts 2025 (Gifford et al., 2025), CineBrain (Gao et al., 2025), and HAD (Zhou et al., 2023), and compare against matched autoregressive and history-only baselines. Beyond one-step decoding, we also treat the model as a generative simulator of brain dynamics via multi-step autoregressive rollout, and assess stability through error accumulation and distribution drift over long horizons. Our contributions are summarized as follows:

- We formulate naturalistic fMRI modeling as a time-aligned multimodal autoregressive prediction task, identifying and addressing the challenge of temporal leakage caused by heterogeneous sampling rates.
- We propose **BrainVista**, a unified multimodal forecasting framework for naturalistic fMRI response prediction, and introduce **Stimulus-to-Brain masking** to enforce a past-only conditioning protocol that prevents temporal leakage and preserves temporal validity.
- We design **Network-wise Tokenizers** as lightweight MLP autoencoders for fMRI self-reconstruction within each functional network and add a **Spatial Mixer Head** to explicitly regulate cross-network information flow.
- We conduct extensive experiments on Algonauts 2025, CineBrain, and HAD under multimodal conditioning, showing that our approach improves long-horizon causal rollout and enables more stable simulation of brain trajectories.

2. Related Work

fMRI Tokenizers. High-dimensional, noisy fMRI motivates compact tokenization for scalable long-horizon sequence learning. Discrete code sequences provide one route (Nishimura et al., 2024; Yang & Wolfers, 2025), while task-aware tokenizers explicitly couple reconstruction with prediction (Zhao et al., 2024). Meanwhile, probabilistic latent tokens capture biological variability via variational learning (Mai et al., 2025; Li et al., 2025). Masked-reconstruction pretraining further supports robustness under partial observability (Qu et al., 2025; Xia et al., 2025). Tokenization thus shapes robustness and transfer beyond mere compression.

Brain Foundation Models. Brain foundation models learn general-purpose neural representations via large-scale neuroimaging pretraining and transfer. Brain-JEPA uses joint-embedding predictive learning with spatiotemporal masking and gradient-based spatial positioning (Dong et al., 2024), while Brain Harmony (BrainHarmonix) encodes morphology and function as compact 1D tokens and supports heterogeneous time (Dong et al., 2025). BrainLM models fMRI dynamics with self-supervised masked prediction (Ortega Caro et al., 2024), and efficiency-oriented variants

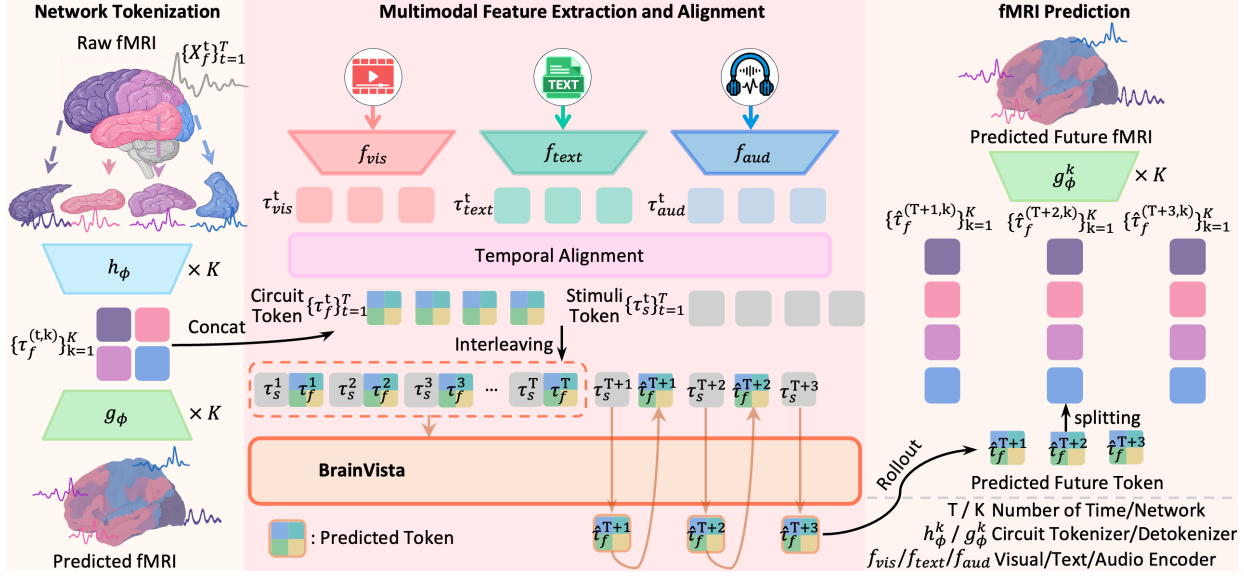


Figure 2. Framework of BrainVista. Time-aligned multimodal features are aggregated into stimuli tokens τ_s^t . Parcel-wise fMRI is encoded and decoded by network-specific tokenizers pretrained via self-reconstruction into fMRI circuit tokens τ_f^t , to preserve functional specificity and support cross-subject alignment. An interleaved, time-aligned token sequence is fed into BrainVista to forecast future fMRI circuit tokens and decode them back to fMRI, pairing stimulus context with the corresponding brain state at each time step. Details of the Stimulus-to-Brain masking and the Spatial Mixer Head are illustrated in Fig. 3.

explore atlas-free or low-memory voxel-level pretraining (Wang et al., 2025b). Generative objectives offer complementary signals including concept-conditioned synthesis (Bao et al., 2025; Wei et al., 2025).

Multimodal Stimulus-Brain Modeling. Naturalistic movie paradigms motivate temporally aligned multimodal modeling of brain activity. TRIBE predicts whole-brain responses from aligned video, audio, and text features (d’Ascoli et al., 2025), while SynBrain models one-to-many mappings via probabilistic learning (Mai et al., 2025). Dynamic subject-aware routing addresses inter-subject variability (Yin et al., 2025), and Algonauts 2025 enables large-scale evaluation under realistic temporal structure (Gifford et al., 2025). Related work also studies stimulus decoding and reconstruction, including diffusion-based reconstruction and unified multimodal decoding (Scotti et al., 2024; Xia et al., 2024; Takagi & Nishimoto, 2023; Scotti et al., 2023). In contrast, we focus on time-aligned causal prediction conditioned on brain history and contemporaneous exogenous context, enabling long-horizon rollout and temporally consistent evaluation (Paugam et al., 2024).

3. Methodology

We cast naturalistic fMRI modeling as time-aligned multimodal next-token forecasting under a past-only constraint, where open-loop rollout iterates a learned one-step transition. In Section 3.1, we define the task, notation, and causal evaluation protocol. In Section 3.2, we form stimulus tokens by encoding video, audio, and text with frozen en-

coders and aggregating them onto the fMRI grid. In Section 3.3, we compress parcel-wise fMRI into compact circuit tokens via network-wise tokenizer-detokenizer pairs, respecting cortical heterogeneity and stabilizing long-horizon prediction. In Section 3.4, we interleave stimulus and circuit tokens for causal step-wise prediction with a shared temporal Transformer, using Stimulus-to-Brain masking to block future stimulus access and a Spatial Mixer Head to control cross-network mixing without blurring functional boundaries. Finally, Section 3.5 describes tokenizer reconstruction and next-token prediction objectives.

3.1. Problem Setup and Notation

Causal Brain Dynamics as Autoregressive Forecasting.

Naturalistic fMRI captures a time-evolving cortical state driven jointly by intrinsic dynamics and time-ordered sensory evidence. This evolution is modeled as a causal state transition on a tokenized sequence, such that forward simulation reduces to repeated one-step prediction under past-only conditioning. For each subject and run, a time-indexed sequence is defined on the fMRI sampling grid: at time t , prediction conditions on a brain representation derived from the parcel-wise measurement $x^t \in \mathbb{R}^p$ (with p atlas parcels) and an aligned stimulus representation s^t obtained from timestamped multimodal features, yielding the next cortical state at $t+1$.

Autoregressive Objective. Given the aligned sequences, our goal is to learn a one-step transition. We parameterize this transition with a predictor f_θ that forecasts the next

cortical state from past brain history together with an exogenous stimulus stream that is assumed observed at inference, using features available up to the current prediction step. Concretely, at time t the one-step forecast is defined as:

$$\hat{x}^{t+1} = f_\theta(x^{\leq t}, s^{\leq t+1}), \quad (1)$$

where x^t denotes the ground-truth cortical state at time t and \hat{x}^t denotes the predictor output. We use $x^{\leq t} = \{x^1, \dots, x^t\}$ and $s^{\leq t+1} = \{s^1, \dots, s^{t+1}\}$, where s^t denotes the aligned stimulus representation at time t . An H -step rollout is obtained by recursively applying the same transition to previously predicted states:

$$\hat{x}^{T+h} = f_\theta(\hat{x}^{\leq T+h-1}, s^{\leq T+h}), \quad h = 1, \dots, H, \quad (2)$$

where at each step we condition on the ground-truth stimulus token aligned to that time point, while feeding back predicted brain states. We do not forecast the stimulus stream.

3.2. Stimuli Tokens

Frozen Encoders. We employ fixed pretrained encoders $f_{\text{vis}}, f_{\text{aud}}, f_{\text{text}}$ to map raw video, audio, and text streams $s_{\text{vis}}, s_{\text{aud}}, s_{\text{text}}$ into time-indexed stimulus tokens, producing $\tau_{\text{vis}} \in \mathbb{R}^{d_v}, \tau_{\text{aud}} \in \mathbb{R}^{d_a}$, and $\tau_{\text{text}} \in \mathbb{R}^{d_t}$. d_v, d_a , and d_t denote the embedding dimensionalities of the video, audio, and text stimulus tokens, respectively.

Temporal Alignment. Stimulus tokens are sampled at a higher rate than fMRI, so we downsample them onto the fMRI grid for causal prediction. Let $\tau_m^t \in \mathbb{R}^{d_m}$ denote high-rate tokens for modality $m \in \{\text{vis, aud, text}\}$, and let $\kappa \in \mathbb{N}$ be the stimulus-to-fMRI downsampling factor. We form one fMRI-aligned token per fMRI step by mean-pooling within each bin:

$$\tau_m^t = \frac{1}{\kappa} \sum_{i=0}^{\kappa-1} \tau_m^{\kappa t+i}, \quad t = 1, \dots, T. \quad (3)$$

Shared Stimulus Token. At each time step t , we form a shared stimulus token by concatenating modality tokens and projecting to a common feature space:

$$\tau_s^t = \text{Proj}([\tau_{\text{vis}}^t; \tau_{\text{aud}}^t; \tau_{\text{text}}^t]) \in \mathbb{R}^{d_f}, \quad (4)$$

where $\tau_{\text{vis}}^t, \tau_{\text{aud}}^t$, and τ_{text}^t are the fMRI-aligned visual, audio, and text tokens at time t , $\text{Proj}(\cdot)$ is a learned projection into the shared stimulus space, and d_f denotes the token embedding dimensionality of the temporal Transformer, shared by both stimulus and brain tokens. We denote the length- L stimulus context at time t as:

$$\mathcal{T}_s^t = \{\tau_s^{t-L+1}, \dots, \tau_s^t\}, \quad (5)$$

where L is the context length in time steps and \mathcal{T}_s^t collects the L most recent stimuli tokens up to time t .

3.3. fMRI Circuit Tokens

Network Partition and Normalization. Brain networks exhibit marked functional heterogeneity. Sensory visual cortex is typically more stimulus-driven with faster temporal fluctuations, whereas the default mode network shows slower, internally driven dynamics with stronger low-frequency components and distinct long-range coupling patterns (Yeo et al., 2011; Glasser et al., 2016). This motivates network-aware representations, since a single global compressor can entangle heterogeneous signals and over-smooth network-specific structure (Qiu et al., 2025). Accordingly, we partition the P parcels into K functional networks $\{\mathcal{V}_k\}_{k=1}^K$, where \mathcal{V}_k denotes the parcel set for network k . We follow the Yeo-7 organization and its Schaefer-parcellation mapping for network assignment (Yeo et al., 2011; Schaefer et al., 2018). Given the parcel-wise fMRI vector $x^t \in \mathbb{R}^p$ at time t , we obtain the network sub-vector by indexing:

$$x^{k,t} = x^t[\mathcal{V}_k] \in \mathbb{R}^{p_k}, \quad (6)$$

where p_k is the number of parcels in network k . To reduce run-specific scale shifts while preserving intra-network variance, we apply run-wise, per-network z-scoring by standardizing each parcel dimension of $x^{k,t}$ over time within the run.

Network-wise Tokenizers and Stitched Circuit Tokens. We deploy independent network-wise tokenizer-detokenizer pairs, pretrained via reconstruction and then used to encode fMRI into circuit tokens for the causal predictor. This allows each pair to specialize to its functional network, while keeping the network partition fixed across subjects to preserve token semantics and support cross-subject alignment. Each tokenizer h_ϕ^k and detokenizer g_ϕ^k is a lightweight two-layer MLP. For each network $k \in \{1, \dots, K\}$, we map the parcel-wise fMRI vector $x^{k,t} \in \mathbb{R}^{p_k}$ at time t to a circuit token and reconstruct it:

$$\tau_f^{t,k} = h_\phi^k(x^{k,t}) \in \mathbb{R}^{d_k}, \quad \hat{x}^{k,t} = g_\phi^k(\tau_f^{t,k}) \in \mathbb{R}^{p_k}, \quad (7)$$

where p_k is the number of parcels in network k and d_k is the token dimensionality. We denote the network-token set at time t as $\mathcal{T}_f^t = \{\tau_f^{t,k}\}_{k=1}^K$ and concatenate them to form the whole-brain circuit token $\tau_f^t = [\tau_f^{t,1}; \dots; \tau_f^{t,K}] \in \mathbb{R}^{d_f}$ with $d_f = \sum_{k=1}^K d_k$. This compact latent representation serves as the brain state at time t for temporal modeling and long-horizon forecasting.

3.4. BrainVista: Temporal Causal Transformer with Stimulus-to-Brain Mask

Interleaved Time-aligned Input Sequence. At time step T , we form a temporal context of length L from stitched circuit tokens $\{\tau_f^t\}_{t=T-L+1}^T$ and aligned stimulus tokens $\{\tau_s^t\}_{t=T-L+1}^T$, where $\tau_f^t \in \mathbb{R}^{d_f}$ and $\tau_s^t \in \mathbb{R}^{d_f}$. We interleave them to construct the Transformer input $S_T \in$

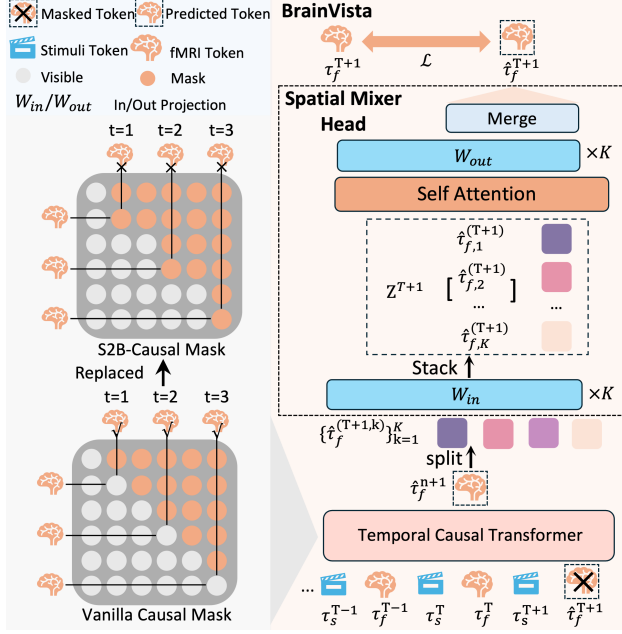


Figure 3. BrainVista core: a temporal causal Transformer with the Stimulus-to-Brain causal masking, followed by a Spatial Mixer Head (network-wise attention) to model cross-network interactions before producing next-step fMRI circuit-token predictions.

$$\mathbb{R}^{2L \times d_f}:$$

$$S^T = (\tau_s^{T-L+1}, \tau_f^{T-L+1}, \dots, \tau_s^T, \tau_f^T) \in \mathbb{R}^{2L \times d_f}. \quad (8)$$

Stimulus-to-brain Causal Mask (S2B). We constrain self-attention with a stimulus-to-brain causal mask $M_T \in \{0, 1\}^{2L \times 2L}$ over the interleaved sequence $S^T \in \mathbb{R}^{2L \times d_f}$ (Fig. 3, lower left), so that circuit-token queries at time t_i attend only to past indices $t_j \leq t_i$ and never to future-aligned stimuli. Formally, M_T is lower-triangular in time and enforces directed mixing: stimulus tokens do not attend to circuit tokens, while circuit tokens may attend to both stimulus and circuit tokens within the allowed past. This avoids non-physical look-ahead and preserves an autoregressive computation graph for open-loop rollout. We feed S^T into a GPT-style Transformer under M_T , take the hidden state at the last circuit-token position, and apply a linear head to predict $\hat{\tau}_f^{T+1} \in \mathbb{R}^{d_f}$.

Spatial Mixer Head for Cross-network Interactions. To model state-dependent cross-network interactions within each step, we treat the network-wise components of the predicted whole-brain token as a length- K sequence and apply a single multi-head self-attention with four heads, whose resulting $K \times K$ attention matrix provides an interpretable summary of pairwise network coupling patterns. We first split the stitched prediction $\hat{\tau}_f^{T+1}$ into K network tokens by slicing it into K tokens with dimensions $\{d_k\}_{k=1}^K$, matching the network-wise token dimensions defined earlier. The split tokens are projected to a shared dimension d_z to form

a length- K token matrix:

$$Z^{T+1} = \text{Stack}\left(\text{Proj}_{\text{in}}\left(\text{Split}(\hat{\tau}_f^{T+1})\right)\right) \in \mathbb{R}^{K \times d_z}. \quad (9)$$

where $\text{Split}(\cdot)$ slices the stitched token into K network components according to the predefined token dimensions $\{d_k\}_{k=1}^K$, and $\text{Proj}_{\text{in}}(\cdot)$ is a linear layer that maps each component to the shared latent size d_z . Multi-head self-attention is then applied over the length- K sequence to model state-dependent cross-network interactions, and the attention outputs are mapped back to network-wise dimensions d_k via Proj_{out} . The resulting network tokens are finally stitched by concatenation to obtain the whole-brain prediction:

$$\hat{\tau}_f^{T+1} = [\hat{\tau}_f^{T+1,1}; \dots; \hat{\tau}_f^{T+1,K}] \in \mathbb{R}^{d_f}. \quad (10)$$

where $\hat{\tau}_f^{T+1,k} \in \mathbb{R}^{d_k}$ denotes the post-mixing token for network k .

3.5. Training Objectives and Optimization

Tokenizer Reconstruction. We pretrain the network-wise tokenizer-detokenizer pairs using a reconstruction objective. For each network k and time step t , the network signal $x^{k,t} \in \mathbb{R}^{p_k}$ is encoded into a circuit token and decoded back to parcel space. The tokenizer loss is:

$$\mathcal{L}_{\text{tok}} = \sum_t \sum_{k=1}^K \left\| x^{k,t} - g_{\phi}^k\left(h_{\phi}^k(x^{k,t})\right) \right\|_2^2. \quad (11)$$

Next-token Prediction. After tokenizer pretraining, we freeze h_{ϕ}^k and train BrainVista with teacher forcing to predict the next stitched circuit token. Let $\tau_f^{t+1} \in \mathbb{R}^{d_f}$ denote the ground-truth stitched token at time $t+1$, and let $\hat{\tau}_f^{t+1} \in \mathbb{R}^{d_f}$ be the model prediction. We minimize:

$$\mathcal{L}_{\text{pred}} = \sum_t \left\| \tau_f^{t+1} - \hat{\tau}_f^{t+1} \right\|_2^2. \quad (12)$$

4. Experiments and Results

4.1. Experimental Setup

Datasets. We evaluate on three naturalistic fMRI benchmarks, Algonauts 2025 (Gifford et al., 2025), CineBrain (Gao et al., 2025), and HAD (Zhou et al., 2023), which differ in stimulus paradigms, preprocessing pipelines, and ROI definitions (Schaefer et al., 2018; Glasser et al., 2016). We follow the official evaluation protocol for Algonauts 2025 (Gifford et al., 2025). For CineBrain and HAD, we construct a forecasting split by partitioning runs at the run level into 80%/20% for train/validation.

Modalities and Network Partition. Across datasets, we use time-aligned multimodal inputs (video, audio, text when

Table 1. Main results under open-loop rollout with a rollout horizon of 20 steps on Algonauts 2025, CineBrain, and HAD. Higher is better for all metrics. Best values are shown in red and second-best values are shown in blue.

Model	Algonauts 2025			CineBrain			HAD		
	<i>r</i>	<i>p_{corr}</i>	Cl _s @Top10	<i>r</i>	<i>p_{corr}</i>	Cl _s @Top10	<i>r</i>	<i>p_{corr}</i>	Cl _s @Top10
TRIBE(d’Ascoli et al., 2025)	0.1379	0.1323	0.6823	0.4742	0.3012	0.8560	0.2685	0.1845	0.7012
MindSimulator(Bao et al., 2025)	0.1432	0.1478	0.6919	0.4856	0.3235	0.8615	0.2710	0.1960	0.7105
BrainLM(Ortega Caro et al., 2024)	0.1191	0.0829	0.6493	0.4633	0.2762	0.8478	0.2465	0.1450	0.6912
BrainJEP(A(Dong et al., 2024)	0.1493	0.0916	0.6812	0.4941	0.2445	0.8455	0.2515	0.2353	0.7321
Brain Harmony(Dong et al., 2025)	0.1867	0.1466	0.7031	0.5397	0.3484	0.8642	0.2642	0.2688	0.7685
BrainVista	0.2183	0.2090	0.7619	0.6315	0.5643	0.9012	0.2739	0.2950	0.7998

Table 2. Rollout performance on HAD at different horizons. Best values are shown in red and second-best values are shown in blue.

Model	<i>H</i> =1		<i>H</i> =10		<i>H</i> =20	
	<i>r</i>	<i>p_{corr}</i>	<i>r</i>	<i>p_{corr}</i>	<i>r</i>	<i>p_{corr}</i>
TRIBE	0.5711	0.5419	0.3150	0.2845	0.2685	0.1845
MindSimulator	0.5782	0.5698	0.3210	0.2960	0.2710	0.1960
BrainLM	0.5695	0.5489	0.2785	0.2250	0.2465	0.1450
BrainJEP(A	0.5971	0.5723	0.2950	0.2810	0.2515	0.2353
Brain Harmony	0.5823	0.5747	0.3085	0.3120	0.2642	0.2688
BrainVista	0.6058	0.6214	0.3278	0.3390	0.2739	0.2950

available) and represent each parcel time series as a brain-token sequence on the fMRI grid. For network-wise reporting, Algonauts 2025 parcels follow the Schaefer seven-network organization derived from Yeo-7 (Schaefer et al., 2018; Yeo et al., 2011). CineBrain ROIs are grouped into two coarse networks (visual vs. auditory) (Gao et al., 2025). HAD ROIs are mapped to Yeo-7 (Yeo et al., 2011).

Stimulus Features and Alignment. Video, audio, and text streams are temporally aligned to the fMRI sampling grid following established dataset protocols (Esteban et al., 2019; Gifford et al., 2025; Gao et al., 2025). We extract features using frozen pretrained encoders: V-JEPA 2 (Assran et al., 2025), Wav2Vec2-BERT (Chung et al., 2021), and Llama 3.2 3B (Grattafiori et al., 2024). Within each temporal window, features are average-pooled, concatenated, and linearly projected to a shared stimulus embedding $\tau_s \in \mathbb{R}^{df}$ with $df=256$.

Training and Evaluation. Unless otherwise stated, we train with AdamW (mixed precision) for 40 epochs using learning rate $\eta=2 \times 10^{-4}$, weight decay 10^{-2} , and batch size 32. We evaluate open-loop autoregressive rollout with context length L and horizon H (past steps provided vs. future steps generated), setting $L=40$ and $H=20$. We report parcel-wise Pearson correlation r and pattern correlation p_{corr} , where p_{corr} emphasizes instantaneous cross-ROI structure and is less sensitive to drift under long-horizon rollout. We additionally report Top-10 Identification Accuracy (Cl_s@Top10) to assess whether the predicted trajectories retain discriminative information for retrieval-based identification. Additional implementation details and hyperparameter settings

are provided in Appendix A.

4.2. Main Results

All methods are evaluated under the same causal open-loop rollout. For competing approaches that are not causal by design, we freeze their pretrained representations and train a lightweight past-only MLP predictor. Inference follows the identical past-only rollout without teacher forcing. All results are the average score of all subjects.

As shown in Table 1, we evaluate multi-step rollout with context length $L=40$ and horizon $H=20$, computing all metrics (r , p_{corr} , and Cl_s@Top10) on the rollout segment only. Across Algonauts 2025, CineBrain, and HAD, BrainVista achieves the best or tied-best performance despite differing ROI parcellations and coordinate spaces, suggesting consistent improvements across brain regions. The margin is typically larger in harder regimes, consistent with improved stability of the learned transition under error accumulation rather than isolated one-step gains. This trend is further corroborated on HAD in Table 2: although all methods degrade as H increases, BrainVista remains best at every horizon and its p_{corr} margin does not collapse, supporting reduced long-horizon drift under causal rollout. Finally, gains in p_{corr} often exceed those in parcel-wise r , consistent with better preservation of instantaneous cross-ROI structure while temporal correlations are more sensitive to phase and drift under long-horizon simulation. Additional quantitative results are reported in Appendix B.

4.3. Visualization Analysis

The visualizations in Fig. 4 provide model-based diagnostics that relate long-horizon rollout stability, temporal attribution, and cross-network interactions to macroscale cortical organization, shown for the first participant (sub01) and the third participant (sub03).

Spatial Heterogeneity. Parcel-wise maps in Fig. 4 (a) show p_{corr} under $H=10$ rollout, and network-level aggregates in Fig. 4 (b) summarize this signal over Yeo-7 systems. Both views reveal heterogeneity: preservation varies across

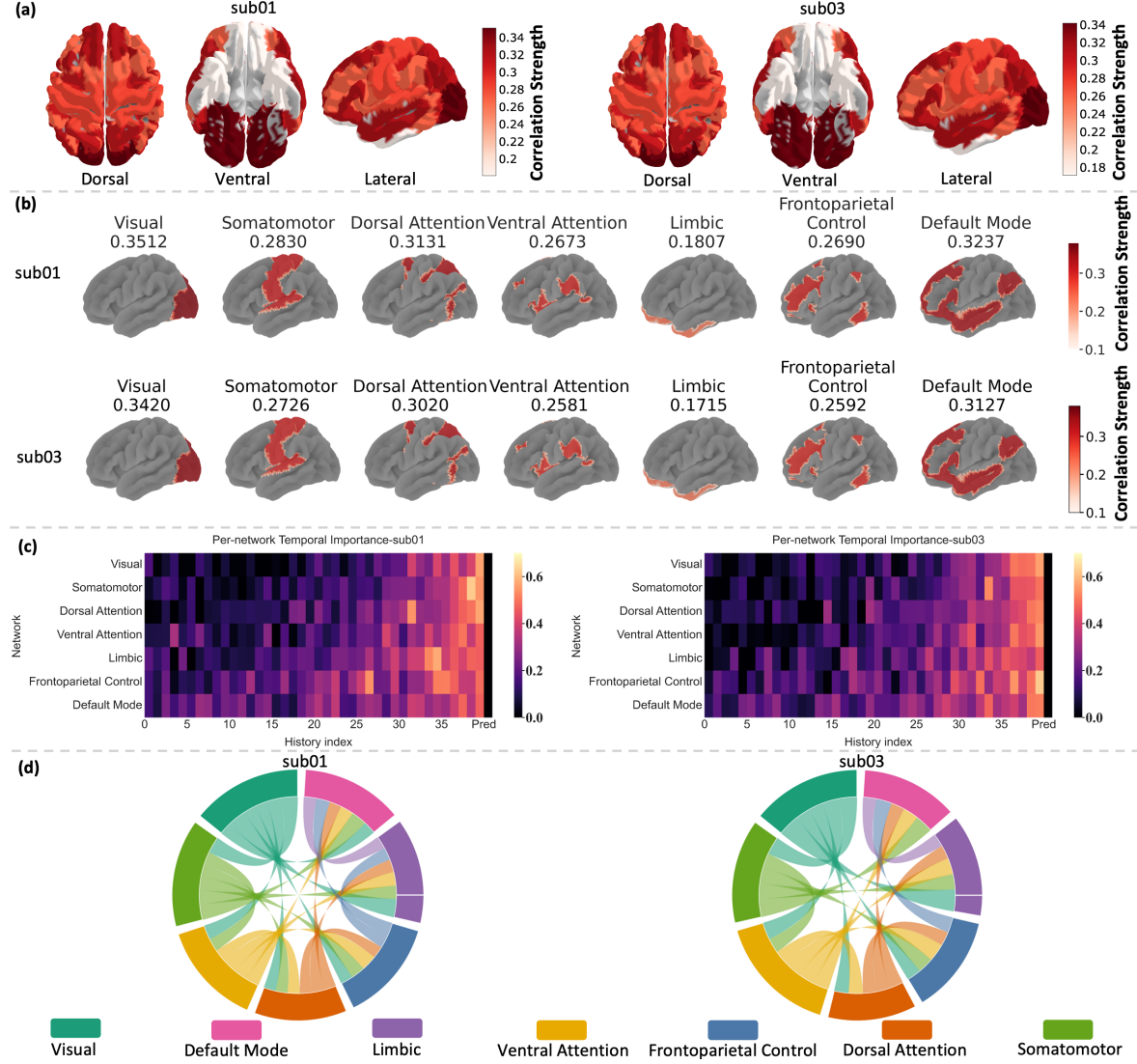


Figure 4. Model-based analyses on Algonauts 2025 aggregated to Yeo-7. Shown for sub01 and sub03. (a) Whole-brain rollout fidelity (p_{corr} , $H=10$) mapped to cortical surfaces (dorsal/ventral/lateral). (b) Network-wise fidelity by aggregating ROIs into Yeo-7. (c) We set one history token to zero at a time and measure the increase in L_2 error, where larger values indicate stronger reliance on that token. (d) Spatial Mixer attention reveals dominant cross-network pathways. We aggregate attention to Yeo-7 network pairs and average across time. Only connections with mean attention ≥ 0.2 are shown. Chord thickness scales with coupling strength.

regions and networks. Sensory-dominant systems (e.g., Visual, SomatoMotor) are preserved, whereas association-heavy systems (e.g., Default, Control, Limbic) are less preserved. An explanation is system-dependent predictability and timescales: unimodal systems are stimulus-driven with faster dynamics, while association systems integrate over longer windows and exhibit stronger variability, amplifying error accumulation under open-loop rollout (Hasson et al., 2008; Lerner et al., 2011; Murray et al., 2014; Honey et al., 2012).

Temporal Reliance. History-token occlusion in Fig. 4(c) reports loss increase as a proxy for temporal reliance. We occlude history tokens at selected lags and measure the loss

increase; larger increases indicate greater reliance. Sensory networks emphasize recent history, attention systems are intermediate, and association networks (Default, Control, Limbic) show broader sensitivity deeper into the past, consistent with hierarchical intrinsic timescales. This provides a mechanistic link to (a,b): longer effective context increases exposure to compounding error under open-loop rollout, lowering long-horizon preservation.

Network Coupling. Chord diagrams summarize strong links from the Yeo-7 aggregation of Spatial Mixer attention in Fig. 4(d), highlighting pathways consistent across participants. Across both participants, coupling is sparse and concentrates on a small set of dominant cross-network

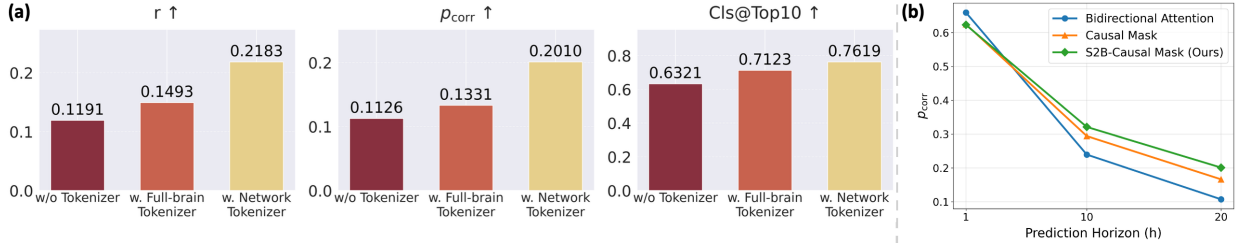


Figure 5. Ablations on Algonauts 2025. (a) **Tokenization granularity:** We compare three input representations: continuous fMRI without tokenization, a shared full-brain tokenizer, and our Network-wise Tokenizers. (b) **Temporal-causality masking:** We compare bidirectional, standard causal, and S2B-causal attention, evaluated by p_{corr} at rollout horizons $H \in \{1, 10, 20\}$.

Table 3. Ablations on Cross-Subject Generalizability. Columns index the training subject, rows index the evaluation subject, and each entry reports p_{corr} .

Model	Test subject	Training subject			
		Sub-01	Sub-02	Sub-03	Sub-05
TRIBE	Sub-01	0.1578	0.1217	0.1241	0.1068
	Sub-03	0.1202	0.1145	0.1398	0.0907
BrainVista	Sub-01	0.2271	0.2003	0.2029	0.1814
	Sub-03	0.2012	0.1994	0.2190	0.1788

Table 4. Ablations on Spatial Mixer Head. All variants share the same architecture and training protocol. We only change the mixing module. Entries report p_{corr} under open-loop rollout at different horizons on Algonauts 2025.

Variant	$H=1$	$H=10$	$H=20$
w/o Spatial Mixer	0.6207	0.3003	0.1706
w. Linear Mixer	0.6252	0.3103	0.1858
w. Spatial Mixer Head (Ours)	0.6303	0.3215	0.2010

pathways, with prominent Control-related interactions consistent with the flexible-hub hypothesis under naturalistic multimodal stimulation. These attention patterns provide an interpretable counterpart to the ablation: a structured mixer supports controlled inter-network flow while avoiding indiscriminate mixing that would blur functional boundaries, amplify drift, and degrade long-horizon spatial-pattern preservation. Additional visualizations are provided in the Appendix C.

4.4. Ablation Studies

Tokenization Granularity. As shown in Fig. 5 (a), network-wise tokenization yields the most consistent gains across datasets and ROI definitions, improving both correlation fidelity and identification under open-loop long-horizon rollout. A shared full-brain latent space must represent ROIs with distinct dynamics and stimulus coupling, which can entangle incompatible factors and hinder causal rollout. By contrast, Network-wise Tokenizers learn more homogeneous within-network codes, producing tokens that are easier to predict and less prone to error compounding, re-

flected by larger gains in p_{corr} and $Cls@Top10$.

Temporal-Causality Masking Across Rollout Horizons. In Fig. 5 (b), p_{corr} decreases as H increases ($1 \rightarrow 10 \rightarrow 20$) for all methods, consistent with compounding error under autoregressive rollout. Enforcing temporally valid attention improves robustness, with larger benefits at longer horizons: bidirectional attention degrades most, a standard causal mask is more stable, and our S2B-causal mask further preserves p_{corr} , supporting that blocking stimulus look-ahead mitigates temporal leakage and anchors multi-step rollout.

Cross-subject Transfer. Table 3 shows that BrainVista improves transfer over TRIBE across all source-target pairings. The gains are consistent across subjects, indicating generalization beyond subject-specific effects. The smaller cross-subject drop suggests that our model encourages system-specific yet more subject-invariant representations, potentially by reducing overfitting to subject noise patterns, although transfer remains asymmetric due to individual variation and heterogeneous signal quality.

Spatial Mixer Head Ablation Under Causal Evaluation. Table 4 isolates the mixing design with a fixed backbone. The Spatial Mixer Head achieves the best p_{corr} across horizons, and its margin grows with H (e.g., $\sim +17.8\%$ at $H=20$ versus removing the mixer), indicating that structured spatial mixing primarily improves long-horizon stability by reducing error accumulation. This suggests that modeling cross-network interactions becomes increasingly important as rollout extends further into the future. Simple linear mixers yield smaller and less consistent gains. Additional ablations are provided in the Appendix D.

5. Conclusion and Discussion

We presented BrainVista, a causal autoregressive framework for naturalistic fMRI prediction. By enforcing temporally valid stimulus conditioning with a Stimulus-to-Brain mask and modeling cross-network interactions using Network-wise Tokenizers and a Spatial Mixer Head, BrainVista achieves gains over baselines on three benchmarks, with the clearest improvements under long-horizon open-loop rollout. These results also clarify trade-offs of past-only multimodal

forecasting. As the rollout horizon grows, performance inevitably degrades due to compounding error, but BrainVista mitigates drift via temporally consistent conditioning and structured cross-network computation. Dataset heterogeneity and reduced correlation performance in association systems reflect intrinsic challenges of naturalistic fMRI; sustained improvements in these harder settings further support the robustness and interpretability of our design. Future work will explore stronger tokenization/decoding objectives and calibration under distribution shifts to further improve long-horizon stability and cross-dataset generalization.

References

Assran, M. et al. V-JEPA 2: Self-supervised video models enable understanding, prediction and planning. *arXiv preprint arXiv:2506.09985*, 2025.

Bao, G., Zhang, Q., Gong, Z., Wu, Z., and Miao, D. Mind-Simulator: Exploring brain concept localization via synthetic fMRI. In *International Conference on Learning Representations (ICLR)*, 2025.

Brown, T. B., Mann, B., Ryder, N., Subbiah, M., Kaplan, J. D., et al. Language models are few-shot learners. In *Advances in Neural Information Processing Systems (NeurIPS)*, volume 33, pp. 1877–1901, 2020.

Chang, C. H. C., Nastase, S. A., and Hasson, U. Information flow across the cortical timescale hierarchy during narrative construction. *Proceedings of the National Academy of Sciences*, 119(51):e2209307119, 2022. doi: 10.1073/pnas.2209307119.

Chung, Y., Zhang, Y., Han, W., Chiu, C., Qin, J., Pang, R., and Wu, Y. W2v-bert: Combining contrastive learning and masked language modeling for self-supervised speech pre-training. In *IEEE Automatic Speech Recognition and Understanding Workshop (ASRU)*, pp. 244–250, 2021.

Clark, A. Whatever next? predictive brains, situated agents, and the future of cognitive science. *Behavioral and Brain Sciences*, 36(3):181–204, 2013.

Darvishi Bayazi, M. J., Ghonia, H., Riachi, R., Aristimunha, B., Khorasani, A., Arefin, M. R., Darabi, A., Dumas, G., and Rish, I. General-purpose brain foundation models for time-series neuroimaging data. In *NeurIPS 2024 Workshop on Time Series Analysis and Learning Models (TSALM)*, October 2024.

d’Ascoli, S., Rapin, J., Benchetrit, Y., Banville, H., and King, J.-R. TRIBE: TRImodal brain encoder for whole-brain fMRI response prediction. In *International Conference on Learning Representations (ICLR)*, 2025.

Demirtaş, M., Burt, J. B., Helmer, M., Ji, J. L., Adkinson, B. D., Glasser, M. F., Van Essen, D. C., Sotiroopoulos, S. N., Anticevic, A., and Murray, J. D. Hierarchical heterogeneity across human cortex shapes large-scale neural dynamics. *Neuron*, 101(6):1181–1194, 2019.

Dong, Z., Li, R., Wu, Y., Nguyen, T. T., Chong, J. S. X., Ji, F., Tong, N. R. J., Chen, C. L. H., and Zhou, J. H. Brain-JEPA: Brain dynamics foundation model with gradient positioning and spatiotemporal masking. In *Advances in Neural Information Processing Systems (NeurIPS)*, 2024.

Dong, Z., Li, R., Chong, J. S. X., Dehestani, N., Teng, Y., Lin, Y., Li, Z., Zhang, Y., Xie, Y., Ooi, L. Q. R., Yeo, B. T. T., and Zhou, J. H. Brain Harmony: A multimodal foundation model unifying morphology and function into 1D tokens. In *Advances in Neural Information Processing Systems (NeurIPS)*, 2025.

Esteban, O. et al. fMRIprep: A robust preprocessing pipeline for functional MRI. *Nature Methods*, 16(1): 111–116, 2019.

Finn, E. S., Shen, X., Scheinost, D., Rosenberg, M. D., Huang, J., Chun, M. M., Papademetris, X., and Constable, R. T. Functional connectome fingerprinting: Identifying individuals using patterns of brain connectivity. *Nature Neuroscience*, 18(11):1664–1671, 2015.

Friston, K. A theory of cortical responses. *Philosophical Transactions of the Royal Society B: Biological Sciences*, 360(1456):815–836, 2005.

Gao, J., Liu, Y., Yang, B., Feng, J., and Fu, Y. CineBrain: A large-scale multi-modal brain dataset during naturalistic audiovisual narrative processing. *arXiv preprint arXiv:2503.06940*, 2025.

Geweke, J. Measurement of linear dependence and feedback between multiple time series. *Journal of the American Statistical Association*, 77(378):304–313, 1982.

Gifford, A. T., Bersch, D., St-Laurent, M., Pinsard, B., Boyle, J., Bellec, L., Oliva, A., Roig, G., and Cichy, R. M. The Algonauts Project 2025 challenge: How the human brain makes sense of multimodal movies. *arXiv preprint arXiv:2501.00504*, 2025.

Glasser, M. F., Coalson, T. S., Robinson, E. C., Hacker, C. D., Harwell, J., Yacoub, E., Ugurbil, K., Andersson, J., Beckmann, C. F., Jenkinson, M., Smith, S. M., and Van Essen, D. C. A multi-modal parcellation of human cerebral cortex. *Nature*, 536(7615):171–178, 2016.

Granger, C. W. J. Investigating causal relations by econometric models and cross-spectral methods. *Econometrica*, 37(3):424–438, 1969.

Grattafiori, A., Dubey, A., Jauhri, A., Pandey, A., Kadian, A., et al. The llama 3 herd of models. *arXiv preprint arXiv:2407.21783*, 2024.

Gratton, C., Laumann, T. O., Nielsen, A. N., Greene, D. J., Gordon, E. M., Gilmore, A. W., Nelson, S. M., Coalson, R. S., Snyder, A. Z., Schlaggar, B. L., Dosenbach, N. U. F., and Petersen, S. E. Functional brain networks are dominated by stable group and individual factors, not cognitive or daily variation. *Neuron*, 98(2):439–452, 2018.

Hasson, U., Yang, E., Vallines, I., Heeger, D. J., and Rubin, N. A hierarchy of temporal receptive windows in human cortex. *Journal of Neuroscience*, 28(10):2539–2550, 2008.

Honey, C. J., Thesen, T., Donner, T. H., Silbert, L. J., Carlson, C. E., Devinsky, O., Doyle, W. K., Rubin, N., Heeger, D. J., and Hasson, U. Slow cortical dynamics and the accumulation of information over long timescales. *Neuron*, 76(2):423–434, 2012.

Lahner, B., Dwivedi, K., Iamshchinina, P., et al. Modeling short visual events through the BOLD moments video fmri dataset and metadata. *Nature Communications*, 15: 6241, 2024. doi: 10.1038/s41467-024-50310-3.

Lerner, Y., Honey, C. J., Silbert, L. J., and Hasson, U. Topographic mapping of a hierarchy of temporal receptive windows using a narrated story. *Journal of Neuroscience*, 31(8):2906–2915, 2011.

Li, Y., Xu, L., Zuo, L., Chang, Y., Ding, Z., Anderson, A. W., Schilling, K. G., Gore, J. C., and Gao, Y. BrainVAE: Exploring the role of white matter BOLD in preclinical Alzheimer’s disease classification. *bioRxiv*, 2025.

Liu, Y., Hu, T., Zhang, H., Wu, H., Wang, S., Ma, L., and Long, M. itransformer: Inverted transformers are effective for time series forecasting. In *International Conference on Learning Representations (ICLR)*, 2024.

Liu, Y., Qin, G., Huang, X., Wang, J., and Long, M. TIMER-XL: Long-context transformers for unified time series forecasting. In *International Conference on Learning Representations (ICLR)*, 2025.

Logothetis, N. K., Pauls, J., Augath, M., Trinath, T., and Oeltermann, A. Neurophysiological investigation of the basis of the fMRI signal. *Nature*, 412(6843):150–157, 2001.

Mai, W., Wu, J., Zhu, Y., Yao, Z., Zhou, D., Luo, A. F., Zheng, Q., Ouyang, W., and Song, C. SynBrain: Enhancing visual-to-fMRI synthesis via probabilistic representation learning. In *Advances in Neural Information Processing Systems (NeurIPS)*, 2025.

Murray, J. D., Bernacchia, A., Roy, N. A., Constantinidis, C., Romo, R., and Wang, X.-J. A hierarchy of intrinsic timescales across primate cortex. *Nature Neuroscience*, 17(12):1661–1663, 2014.

Nie, Y., Nguyen, N. H., Sinthong, P., and Kalagnanam, J. R. A time series is worth 64 words: Long-term forecasting with transformers. In *International Conference on Learning Representations (ICLR)*, 2023.

Nishimura, Y., Sawayama, M., Yamashita, A., Nakayama, H., and Amano, K. BrainCodec: Neural fMRI codec for the decoding of cognitive brain states. *arXiv preprint arXiv:2410.04383*, 2024.

Ortega Caro, J., Fonseca, A. H. d. O., Rizvi, S. A., Rosati, M., et al. BrainLM: A foundation model for brain activity recordings. In *International Conference on Learning Representations (ICLR)*, 2024.

Paugam, F., Pinsard, B., Lajoie, G., and Bellec, P. A benchmark of individual auto-regressive models in a massive fMRI dataset. *Imaging Neuroscience*, 2:1–23, 2024.

Qiu, W., Huang, Z., Hu, H., Feng, A., Yan, Y., and Ying, R. Mindllm: A subject-agnostic and versatile model for fmri-to-text decoding. In *Proceedings of the 42nd International Conference on Machine Learning (ICML)*, 2025.

Qu, Y., Xia, J., Jian, X., Li, W., Peng, K., Liang, Z., Wu, H., and Liu, Q. Uncovering cognitive taskonomy through transfer learning in masked autoencoder-based fMRI reconstruction. In *International Conference on Human Brain and Artificial Intelligence (HBAI)*, pp. 35–50. Springer, 2025.

Schaefer, A. et al. Local-Global Parcellation of the human cerebral cortex from intrinsic functional connectivity MRI. *Cerebral Cortex*, 28(9):3095–3114, 2018.

Scotti, P., Banerjee, A., Goode, J., Shabalin, S., Nguyen, A., Cohen, E., Dempster, A., Verlinde, N., Yundler, E., Weisberg, D., Norman, K., and Abraham, T. Reconstructing the mind’s eye: fmri-to-image with contrastive learning and diffusion priors. In *Advances in Neural Information Processing Systems (NeurIPS)*, 2023.

Scotti, P. S., Tripathy, M., Torrico, C., Kneeland, R., Chen, T., Narang, A., Santhirasegaran, C., Xu, J., Naselaris, T., Norman, K. A., and Abraham, T. M. MindEye2: Shared-subject models enable fMRI-to-image with 1 hour of data. In *ICLR Workshop Re-Align*, 2024.

Takagi, Y. and Nishimoto, S. High-resolution image reconstruction with latent diffusion models from human brain activity. In *Proceedings of the IEEE/CVF Conference on Computer Vision and Pattern Recognition (CVPR)*, 2023.

Wang, E. Y., Fahey, P. G., Ding, Z., Papadopoulos, S., Ponder, K., Weis, M. A., Chang, A., Muhammad, T., Patel, S., Ding, Z., Tran, D., Fu, J., et al. Foundation model of neural activity predicts response to new stimulus types. *Nature*, 640:470–477, April 2025a.

Wang, M., Xia, J., Ye, W., Liu, E., Peng, K., Feng, J., Liu, Q., and Wen, H. SLIM-Brain: A data- and training-efficient foundation model for fMRI data analysis. *arXiv preprint arXiv:2512.21881*, 2025b.

Wei, X., Zhao, K., Jiao, Y., He, L., and Zhang, Y. A brain graph foundation model: Pre-training and prompt-tuning for any atlas and disorder. *arXiv preprint arXiv:2506.02044*, 2025.

Wu, H., Hu, T., Liu, Y., Zhou, H., Wang, J., and Long, M. Timesnet: Temporal 2d-variation modeling for general time series analysis. In *International Conference on Learning Representations (ICLR)*, 2023.

Xia, W., Charette, R. d., Oztureli, C., and Xue, J.-H. UMBRAE: Unified multimodal brain decoding. In *European Conference on Computer Vision (ECCV)*, 2024.

Xia, W., Zhang, X., Hu, D., Cheng, J., Yu, X., Yin, W., Wu, Z., Wang, L., Lin, W., and Li, G. Triplet longitudinal masked autoencoder for predicting individualized functional connectome development during infancy. *Medical Image Analysis*, 108:103860, 2025.

Yang, Y. and Wolfers, T. Hierarchical characterization of brain dynamics via state space-based vector quantization. *arXiv preprint arXiv:2506.22952*, 2025.

Yeo, B. T. T. et al. The organization of the human cerebral cortex estimated by intrinsic functional connectivity. *Journal of Neurophysiology*, 106(3):1125–1165, 2011.

Yin, X., Zhao, R., and Cai, W. Improving multimodal brain encoding model with dynamic subject-awareness routing. *arXiv preprint arXiv:2510.04670*, 2025.

Zhao, Y., Nie, D., Chen, G., Wu, X., Zhang, D., and Wen, X. TARDRL: Task-aware reconstruction for dynamic representation learning of fMRI. In *International Conference on Medical Image Computing and Computer-Assisted Intervention (MICCAI)*, 2024.

Zhou, M., Gong, Z., Dai, Y., Wen, Y., Liu, Y., Zhen, Z., et al. A large-scale fMRI dataset for human action recognition. *Scientific Data*, 10(1):415, 2023.

A. Experimental Details

We report only the missing implementation details needed to reproduce the numbers in the main paper, without restating dataset protocols or model components already described in the main text. Specifically, we summarize (i) the exact hyperparameters and training options used in our runs and (ii) the full metric protocols that are only briefly described in the main text.

Training and Architecture Hyperparameters. Unless otherwise stated, all variants use context length $L=40$ and are evaluated under open-loop rollout with horizon $H=20$, together with teacher-forced one-step evaluation. The predictor is a Pre-LN Transformer with $d_{\text{model}}=256$, $n_{\text{head}}=8$, and $n_{\text{layer}}=4$, using GELU activations and an FFN expansion ratio of $4\times$. We use absolute positional embeddings for the input sequence. Dropout is set to 0.1. Optimization uses AdamW with learning rate 2×10^{-4} and weight decay 0.01, trained for 40 epochs with batch size 32 and gradient clipping at 0.5. We apply a warmup schedule at the beginning of training. We do not use gradient accumulation. Training uses PyTorch native AMP (mixed precision). Weight decay is not applied to LayerNorm parameters or bias terms.

Tokenizer Configuration. For network-wise tokenization, we train a separate tokenizer per network/brain-region group. Each tokenizer is a single-layer MLP whose token dimension is set to $0.8\times$ the corresponding input ROI-feature dimension for that group. Tokenizers are trained for 50 epochs with learning rate 2×10^{-5} , and then kept fixed during predictor training unless a fine-tuning variant is explicitly stated.

Metric Definitions and Evaluation Protocols. Let $\hat{\mathbf{y}} \in \mathbb{R}^{T \times K}$ and $\mathbf{y} \in \mathbb{R}^{T \times K}$ denote the predicted and ground-truth trajectories over T time steps and K ROIs/parcels. For correlation metrics, we first concatenate trajectories across ROIs and compute a single global score over the concatenated vectors: Pearson correlation r is computed between $\text{vec}(\hat{\mathbf{y}})$ and $\text{vec}(\mathbf{y})$.

Pattern Correlation (p_{corr}). We compute p_{corr} as the average correlation of *spatial patterns* across ROIs at each time step. For each $t \in \{1, \dots, T\}$, let $\hat{\mathbf{y}}_{t,:} \in \mathbb{R}^K$ and $\mathbf{y}_{t,:} \in \mathbb{R}^K$ denote the predicted and ground-truth ROI vectors. We define:

$$p_{\text{corr}} = \frac{1}{T} \sum_{t=1}^T \text{corr}(\hat{\mathbf{y}}_{t,:}, \mathbf{y}_{t,:}), \quad (13)$$

where $\text{corr}(\cdot, \cdot)$ is the Pearson correlation computed across the K ROIs at a fixed time step. This metric emphasizes instantaneous cross-ROI spatial structure and is less sensitive to global phase drift accumulated during long-horizon rollout.

For identification, we compute Cls@Top10 using segments of length 20 time steps: for each query predicted segment, we form a candidate set consisting of ground-truth segments from the same subject but different runs, rank candidates by correlation similarity, and report the fraction of queries whose true match is retrieved within the top-10.

Sequence Boundary Handling. We reset the temporal context at run boundaries and never carry context across runs. For sequence start positions where fewer than L steps of history are available, we discard those positions rather than padding, so that all training and evaluation windows have full context length.

B. Additional Quantitative Results

In addition to the main metrics reported in the main paper (r , p_{corr} , and Cls@Top10) under open-loop rollout, we provide supplementary metrics that probe complementary aspects of predictive quality. The full numerical results are reported in Table 5. These metrics are computed under the same evaluation protocol as the main results (including the same rollout horizon where applicable) and are reported for completeness rather than as alternative optimization targets.

Mean Squared Error (MSE). We report MSE between predicted and ground-truth trajectories as a scale-sensitive measure of point-wise fidelity:

$$\text{MSE} = \frac{1}{TK} \|\hat{\mathbf{y}} - \mathbf{y}\|_2^2, \quad (14)$$

where $\hat{\mathbf{y}}, \mathbf{y} \in \mathbb{R}^{T \times K}$ denote predicted and ground-truth ROI/parcellation trajectories. Compared with correlation-based metrics, MSE penalizes absolute deviations and is more sensitive to amplitude mismatch. Empirically, our method achieves consistently lower MSE, indicating reduced drift during multi-step rollout and improved stability of the predicted trajectories, rather than merely improving rank-based similarity.

Spearman’s Rank Correlation (ρ). We additionally report Spearman’s ρ to measure monotonic agreement between predicted and ground-truth trajectories. Unlike Pearson correlation, ρ is less sensitive to linear rescaling and outliers, and

Table 5. Supplementary metrics under causal rollout evaluation. We additionally report MSE (lower is better, \downarrow), ρ (higher is better, \uparrow), and 2v2 identification accuracy (higher is better, \uparrow) on three benchmarks. Main-text metrics (r , p_{corr} , and $\text{Cls}@\text{Top10}$) are reported in the main tables for readability.

Model	Algonauts 2025			CineBrain			HAD		
	MSE \downarrow	$\rho \uparrow$	2v2 \uparrow	MSE \downarrow	$\rho \uparrow$	2v2 \uparrow	MSE \downarrow	$\rho \uparrow$	2v2 \uparrow
TRIBE	1.372	0.1101	0.7289	0.405	0.7791	0.9715	1.2150	0.2412	0.7356
MIND	1.243	0.1146	0.7312	0.382	0.7834	0.9740	1.1540	0.2488	0.7390
BrainLM	1.243	0.1071	0.7104	0.366	0.7674	0.9690	1.1010	0.2296	0.7213
BrainJEPAP	1.078	0.1338	0.7544	0.281	0.7320	0.9710	0.7843	0.2203	0.7412
BrainHarmony	0.958	0.1729	0.7623	0.243	0.7789	0.9823	0.6980	0.2415	0.8150
BrainVista	0.878	0.2297	0.8524	0.221	0.9305	0.9890	0.6253	0.2573	0.8721

Table 6. Rollout performance at different horizons on Algonauts 2025 and CineBrain. We report Pearson r and pattern correlation p_{corr} under open-loop causal rollout at $H \in \{1, 10, 20\}$. Models match Table 2. The $H=20$ entries are taken from Table 1; $H=1/10$ entries are placeholders to be replaced with actual results (BrainVista p_{corr} on CineBrain is fixed to the provided scale).

Model	Algonauts 2025						CineBrain					
	$H=1$		$H=10$		$H=20$		$H=1$		$H=10$		$H=20$	
	r	p_{corr}	r	p_{corr}	r	p_{corr}	r	p_{corr}	r	p_{corr}	r	p_{corr}
TRIBE	0.3695	0.3545	0.2045	0.1962	0.1379	0.1323	0.7647	0.4857	0.5714	0.3630	0.4742	0.3012
MindSimulator	0.3837	0.3960	0.2124	0.2192	0.1432	0.1478	0.7831	0.5217	0.5852	0.3898	0.4856	0.3235
BrainLM	0.3191	0.2221	0.1767	0.1230	0.1191	0.0829	0.7471	0.4454	0.5583	0.3328	0.4633	0.2762
BrainJEPAP	0.4000	0.2454	0.2214	0.1359	0.1493	0.0916	0.7968	0.3943	0.5954	0.2946	0.4941	0.2445
Brain Harmony	0.5002	0.3928	0.2769	0.2174	0.1867	0.1466	0.8703	0.5618	0.6504	0.4198	0.5397	0.3484
BrainVista	0.5849	0.5600	0.3238	0.3100	0.2183	0.2090	0.9000	0.9100	0.7610	0.6800	0.6315	0.5643

therefore serves as a robustness check for the reported gains. We observe that the improvements persist under ρ , suggesting that the gains are not driven by a small set of extreme values and that the predicted dynamics better preserve the relative temporal ordering of neural responses.

Two-versus-Two Identification (2v2). We include the 2v2 identification score as an alternative retrieval-style metric that evaluates discriminability under segment-level matching. Following the standard protocol, we randomly sample candidate pairs within each subject using cross-run candidates and measure how often the predicted segment is more similar (by correlation) to its true match than to the distractor. Compared with $\text{Cls}@\text{Top10}$, 2v2 is less dependent on the size of the candidate pool and provides a complementary view of whether rollout predictions retain segment-specific information. The consistent gains under 2v2 support the conclusion that improvements in correlation fidelity translate into improved identification behavior, rather than being a purely smoothing effect.

Full Horizon Breakdown on Algonauts 2025 and CineBrain. To complement Table 2 (HAD), Table 6 reports the same open-loop causal rollout evaluation on Algonauts 2025 and CineBrain at $H \in \{1, 10, 20\}$ using the identical set of competing models. Across both datasets, performance decreases as the rollout horizon increases, reflecting compounding error under open-loop prediction.

Network-level p_{corr} Breakdown across Subjects. Table 7 reports the Yeo-7 network-averaged p_{corr} values corresponding to the maps in Fig. 4(b) under $H=10$ rollout. A consistent cross-subject profile emerges. Visual and Default modes achieve the highest pattern fidelity (Visual: 0.3275–0.3512; Default: 0.3015–0.3237), whereas Limbic remains the most challenging system (0.1585–0.1807). Attention and control networks fall in between (Dorsal Attention: 0.2835–0.3131; Ventral Attention: 0.2415–0.2673; Frontoparietal/Control: 0.2465–0.2690), matching the spatial heterogeneity described in Sec. 4.3. Inter-subject variation is moderate in absolute scale (the mean across the seven networks ranges from 0.2587 to 0.2840), while the relative ordering of networks is largely preserved, suggesting stable system-level behavior under long-horizon rollout.

Additional Test Subjects for Cross-subject Generalization. Table 8 reports cross-subject generalizability on the remaining two test subjects (Sub-02 and Sub-05) to complement the main-paper table. We follow the same protocol and report p_{corr} for each (training subject, test subject) pair. The overall pattern is consistent with the main results: BrainVista shows strong gains over the baseline across training subjects, and the improvements persist under heterogeneous train–test combinations rather than being driven by a single favorable subject pairing.

Table 7. Yeo-7 network-level p_{corr} under $H=10$ rollout. Values summarize the network-aggregated maps shown in Fig. 4(b) for four subjects.

Subject	Visual	SomMot	DorsAttn	VentrAttn	Limbic	FPN/Control	Default
sub01	0.3512	0.2830	0.3131	0.2673	0.1807	0.2690	0.3237
sub02	0.3381	0.2605	0.2977	0.2505	0.1695	0.2595	0.3092
sub03	0.3420	0.2726	0.3020	0.2581	0.1715	0.2592	0.3127
sub05	0.3275	0.2520	0.2835	0.2415	0.1585	0.2465	0.3015

Table 8. Additional cross-subject generalizability on Sub-02 and Sub-05. Columns index the training subject, rows index the evaluation subject, and each entry reports p_{corr} .

Model	Test subject	Training subject			
		Sub-01	Sub-02	Sub-03	Sub-05
TRIBE	Sub-02	0.1182	0.1316	0.1210	0.1094
	Sub-05	0.0957	0.1013	0.0938	0.1024
BrainVista	Sub-02	0.1941	0.2087	0.1968	0.1875
	Sub-05	0.1793	0.1826	0.1765	0.1990

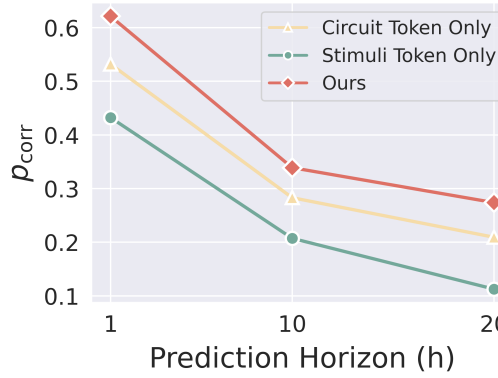


Figure 6. Ablation on token types under causal rollout. We compare using only circuit tokens, only stimulus tokens, and BrainVista (both token streams) across prediction horizons. Performance is measured by p_{corr} (higher is better).

C. Additional Visualizations

Parcel-wise Rollout Fidelity Map. For each subject, we run open-loop causal rollout at a fixed horizon (matching the main paper), compute p_{corr} at each time step as the Pearson correlation between predicted and ground-truth ROI activity vectors, and then average over time to obtain a single score per parcel. We visualize these parcel-level scores on the cortical surface using a shared colormap range across subjects to enable direct comparison.

Yeo-7 Network Summary. We aggregate the parcel-wise p_{corr} scores to Yeo-7 systems by averaging scores over parcels assigned to each network. The resulting seven values are displayed as a network-level summary (with the same ordering and scaling as in the main paper), highlighting consistent differences between sensory and association systems.

History-token Occlusion. To estimate temporal reliance, we perform history-token occlusion at different lags by masking (or zeroing) the history tokens corresponding to a specific lag while keeping all other inputs unchanged, and re-evaluate the prediction loss under the same causal protocol. We report the induced loss increase relative to the unoccluded setting; larger increases indicate stronger reliance on that lagged context.

Spatial Mixer Attention Coupling. We extract attention weights from the Spatial Mixer Head, map them to ROI-to-ROI (or network-to-network) interaction scores by averaging over time and layers (and heads if applicable), and then aggregate to Yeo-7 systems to obtain a compact coupling matrix. We visualize the strongest connections with a chord diagram, using a consistent thresholding rule across subjects to highlight structured, non-uniform cross-network pathways.

Subject-level Diagnostics. Fig. 7 provides additional subject-level visualizations to complement the main-paper diagnostics.

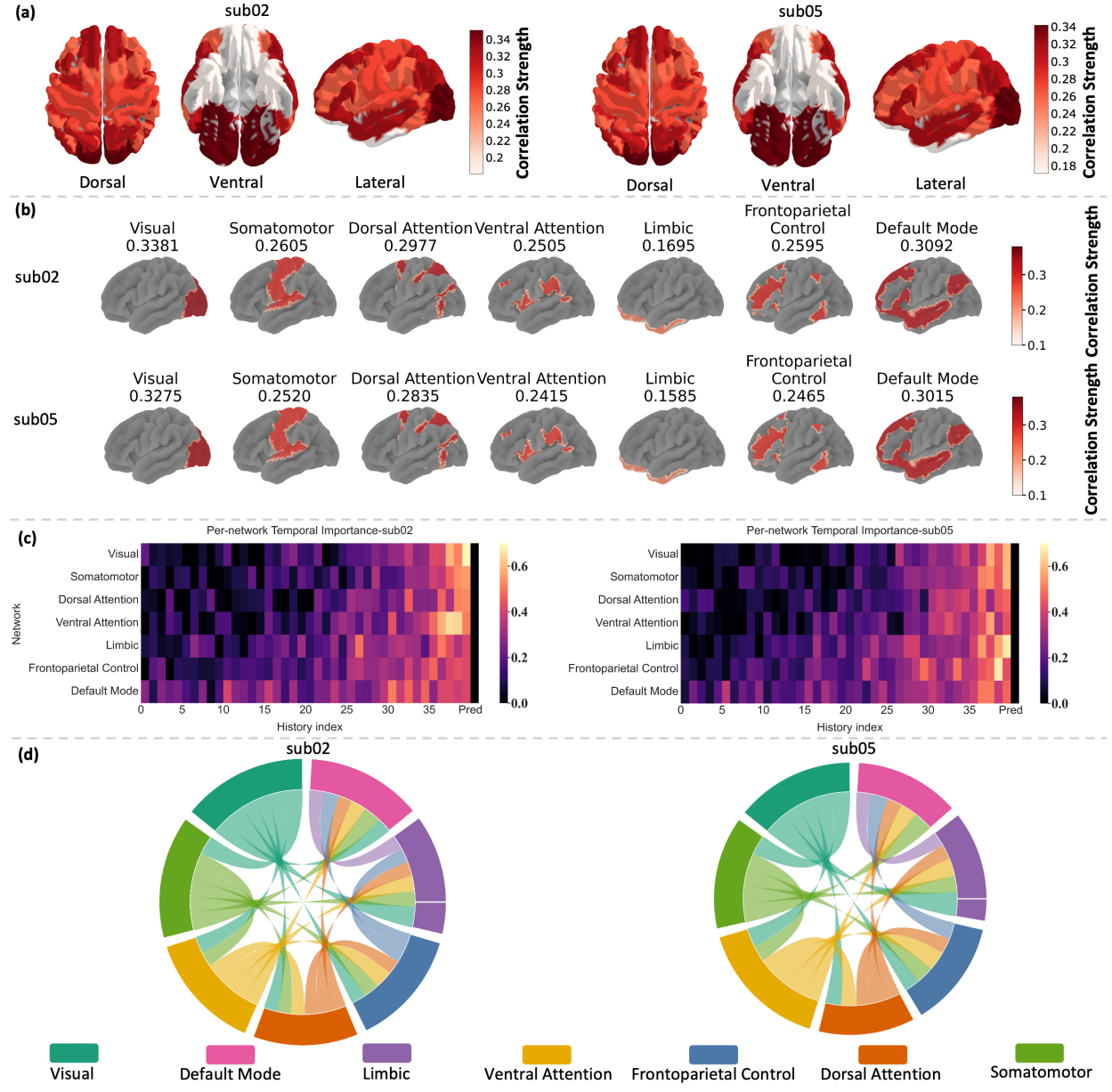


Figure 7. Additional model-based diagnostics on Algonauts 2025 aggregated to Yeo-7, shown for sub02 and sub05. Panels follow the same protocol as Fig. 5 in the main text: (a) whole-brain rollout fidelity (p_{corr} , open-loop; rendered from dorsal/ventral/lateral views), (b) network-wise aggregation over Yeo-7 systems, (c) token-occlusion sensitivity over the history context, and (d) cross-network coupling summarized from the Spatial Mixer attention.

While the main text focuses on a subset of subjects for clarity, here we report the remaining subjects using the same visualization pipeline and scaling. Across subjects, the qualitative patterns are consistent: (i) the spatial distribution of rollout fidelity remains heterogeneous rather than uniform, (ii) network-level summaries preserve the same relative ordering of easier vs. harder networks, and (iii) the history-token occlusion analysis shows a stable dependence on recent context rather than isolated peaks at single time steps. Finally, the attention-based coupling visualization from the Spatial Mixer exhibits similarly structured, non-uniform connectivity across subjects, suggesting that the qualitative behavior observed in the main paper is not driven by a single subject-specific artifact.

Table 9. Ablation: Frozen stimulus encoders for constructing stimulus tokens. All settings are identical except the pretrained frozen encoder used to extract multimodal stimulus features on H=20.

Frozen stimulus encoder(s)	$r \uparrow$	$p_{\text{corr}} \uparrow$	Cl@Top10 \uparrow
Baseline (main paper encoders)	0.232	0.208	0.782
ImageBind (frozen)	0.224	0.199	0.764
Qwen Omni 2.5 (frozen)	0.214	0.188	0.742

Table 10. Tokenizer reconstruction ablation (standalone pretraining, not using BrainVista). Reconstruction correlation r is reported. BrainVAE variants follow SynBrain (Mai et al., 2025).

Family	Objective	$r \uparrow$
MLP	AE	0.834
MLP	VAE	0.507
BrainVAE	AE	0.814
BrainVAE	VAE	0.797

D. Additional Ablations

Tokenizer Composition in the Input Sequence. Fig. 6 ablates which token types are provided in the interleaved sequence. Using stimulus tokens alone consistently underperforms the full model, indicating that exogenous inputs are insufficient to maintain accurate rollout without the autoregressive continuity carried by past brain-state tokens. Conversely, using brain/circuit tokens alone also degrades performance, suggesting that removing stimulus conditioning makes the predictor more prone to drift as errors compound over multi-step rollout. The combined setting yields the best correlation fidelity and identification accuracy, and the gap widens at longer horizons, supporting the role of stimulus conditioning in stabilizing long-horizon forecasting while preserving segment-level discriminability.

Frozen Stimulus Encoders for Constructing Stimulus Tokens. Table 9 further isolates the impact of the pretrained frozen encoders used to extract multimodal stimulus features. All settings are kept identical, and we only replace the frozen encoder(s) for constructing stimulus tokens. We observe a clear ordering across r , p_{corr} , and Cl@Top10: the baseline encoders used in the main paper perform best, ImageBind is slightly worse, and Qwen Omni 2.5 is the weakest. This indicates that, beyond the presence of stimulus conditioning (Fig. 6), the quality and temporal specificity of extracted stimulus representations materially affect causal rollout, improving both trajectory fidelity (correlation metrics) and segment discriminability (identification metrics).

Effect of Combining Circuit and Stimulus Tokens. Fig. 6 shows that both ablated variants degrade as the rollout horizon increases, but the degradation is substantially more severe when either token stream is removed. Using circuit tokens only preserves some autoregressive continuity yet lacks direct conditioning on the ongoing stimulus, while using stimulus tokens only ignores endogenous brain dynamics and yields the weakest long-horizon stability. In contrast, BrainVista consistently attains the best p_{corr} at all horizons and maintains a larger margin at longer horizons, indicating that integrating stimulus history with circuit-state tokens is critical for mitigating error accumulation in open-loop prediction.

Tokenizer Reconstruction Ablation. To isolate the effect of tokenizer design from the downstream causal predictor, we additionally compare several tokenizers using standalone reconstruction performance, i.e., without training or evaluating BrainVista. Table 10 reports the reconstruction correlation r for four variants that differ in both architecture family (a plain MLP tokenizer vs. the BrainVAE-style tokenizer) and training objective (AE vs. VAE). BrainVAE variants follow the probabilistic representation learning setup in SynBrain (Mai et al., 2025). Overall, the deterministic AE objectives yield substantially stronger reconstruction than the corresponding VAE objectives in this setting, while the BrainVAE-AE and BrainVAE-VAE remain competitive relative to the MLP baselines. These results serve as an auxiliary diagnostic of representation capacity at the tokenizer level and should not be conflated with end-to-end forecasting quality, which depends on the causal rollout model and multimodal conditioning.

Modality Ablation. To quantify the contribution of each stimulus modality, we remove video, audio, or text inputs at inference while keeping the architecture and training protocol unchanged, and evaluate open-loop causal rollout at multiple horizons on Algonauts 2025 (Table 11). The full multimodal setting consistently performs best, while dropping any modality degrades p_{corr} , with the largest decline observed when video is removed, suggesting that visual context contributes most to

Table 11. Modality ablation on Algonauts 2025 under causal rollout. We remove one stimulus modality at inference while keeping the model and training protocol unchanged, and report p_{corr} under open-loop rollout at different horizons. Higher is better.

Variant	$H=1$	$H=10$	$H=20$
All (V+A+T)	0.560	0.310	0.209
w/o Video (A+T)	0.510	0.270	0.184
w/o Audio (V+T)	0.540	0.295	0.200
w/o Text (V+A)	0.538	0.293	0.198
Video only (V)	0.485	0.255	0.175
Audio only (A)	0.455	0.235	0.165
Text only (T)	0.440	0.228	0.160

preserving cross-ROI spatial patterns under long-horizon rollout. Single-modality variants further confirm that multimodal conditioning is important for stable rollout.